Detection and correction of rigid patient motion in SPECT with exponential data consistency conditions

My Hoang Hoa Bui, Antoine Robert, Simon Rit, Ane Etxebeste

Detection and correction of rigid patient motion in SPECT with exponential data consistency conditions

My Hoang Hoa Bui[1], Antoine Robert[1], Simon Rit[1], and Ane Etxebeste[1]

[1]INSA-Lyon, Université Claude Bernard Lyon 1, CNRS, Inserm, CREATIS UMR 5220, U1294, F-69373, Lyon, France

Abstract Targeted radionuclide therapy has gained an increasingly important role in cancer treatment in recent years, in which molecular imaging techniques such as SPECT can be employed to plan and monitor the treatment. However, rigid patient motion is degrading the quality of SPECT images and may impact the treatment planning. It has been recently proposed to use exponential data consistency conditions — equations describing the redundancy of exponential SPECT measurements — to detect and correct for patient motion. This study aimed at developing a data consistency-based method to estimate and correct for rigid patient motion during SPECT acquisitions. The proposed method was evaluated on Monte Carlo simulated data of a liver patient. The method led to a significant improvement in the image quality. An activity recovery coefficient above 95% with respect to the reconstructed images from motion-free projections was obtained across all tested cases. In particular, for a motion in the middle of the acquisition, the activity recovery coefficient was improved from 66 % (non-corrected projections) to 99% (motion-corrected projections).

1 Introduction

Targeted radionuclide therapy is a favorable option in cancer treatment thanks to its ability to selectively deliver radiation to cancerous cells, thus minimizing toxicity on surrounding healthy tissues [1]. Functional imaging such as single photon emission computed tomography (SPECT) can be used to optimize the treatment plan, i.e. to adjust the amount of injected radionuclides [2–4].

After injecting the patient, the SPECT scanner collects projections of the emission map with one or several rotating gamma cameras. However, data acquisition requires a long time, typically 5 to 40 minutes. During this time, rigid patient motion is likely to occur [5], potentially leading to artifacts in reconstructed images [6].

Exponential data consistency conditions (eDCCs) are mathematical equations that describe redundancies among measurements modeled by a linear operator called the exponential Radon transform. Recently, Wells and Clackdoyle showed the feasibility of using eDCCs to align the attenuation map to the emission map in pinhole cardiac SPECT [7]. In [8], Robert *et al* studied the ability of eDCCs to detect motion on realistic simulated data in parallel SPECT.

To our knowledge, motion compensation in SPECT exploiting eDCCs exclusively has not been studied yet. This study aimed at employing eDCCs for automated estimation and correction of patient motion, requiring solely the acquired projections and the attenuation map of the patient.

2 Materials and method

2.1 Exponential data consistency conditions

The exponential Radon transform is a two-dimensional (2D) operator and eDCCs can be expressed in 2D. Throughout this study, we express them in a three-dimensional (3D) space for deriving the correction of 3D motions but their 2D expression can be obtained by dropping the third coordinate.

Consider a 3D radioactivity distribution f and an attenuating medium μ. The ideal measurement of f in parallel SPECT geometry can be modeled by the attenuated Radon transform:

$$p_\mu(\theta,s,z) = \int_{-\infty}^{+\infty} f(s\mathbf{u}_\theta + t\mathbf{v}_\theta + z\mathbf{e}_z) \exp\left(-\int_t^{+\infty} \mu(s\mathbf{u}_\theta + t'\mathbf{v}_\theta + z\mathbf{e}_z)\,\mathrm{d}t'\right)\mathrm{d}t \quad (1)$$

where $\mathbf{u}_\theta = (\cos\theta, \sin\theta, 0)$, $\mathbf{v}_\theta = (-\sin\theta, \cos\theta, 0)$ and $\mathbf{e}_z = (0,0,1)$.

Assuming that there is a known convex region K where the attenuation is constant, i.e. $\mu(x,y,z) = \mu_0$ if $(x,y,z) \in K$, and all radioactivity is encompassed inside K, the exponential projections $p(\theta,s,z)$ can be derived from $p_\mu(\theta,s,z)$ by a point-wise conversion, as:

$$p(\theta,s,z) = p_\mu(\theta,s,z)C(\theta,s,z). \quad (2)$$

The conversion factor $C(\theta,s,z)$ was introduced in [9]

$$C(\theta,s,z) = \exp\left(\tau_{\theta,s,z}\mu_0 + \int_{\tau_{\theta,s,z}}^{+\infty} \mu(s\mathbf{u}_\theta + t'\mathbf{v}_\theta + z\mathbf{e}_z)\,\mathrm{d}t'\right) \quad (3)$$

with $\tau_{\theta,s,z}$ the point along the integral line towards the detector where the photon leaves the convex region K.

Range conditions of the exponential Radon transform, known as eDCCs, state that two projections at θ_i and θ_j which are not 180° apart ($\theta_i - \theta_j \neq \pi\,[2\pi]$) are consistent if and only if

$$P(\theta_i, \sigma_{ij}, z) = P(\theta_j, \sigma_{ji}, z) \quad (4)$$

with $P(\theta,\sigma,z) = \int_{-\infty}^{+\infty} p(\theta,s,z)e^{\sigma s}\,\mathrm{d}s$ the two-sided Laplace transform of projection line $p(\theta,\cdot,z)$ and $\sigma_{ij} = -\sigma_{ji} = \mu_0 \tan((\theta_i - \theta_j)/2)$.

2.2 Motion simulation

Using a validated GATE model of the Symbia Intevo Bold scanner [10, 11], we simulated a liver radioembolization patient using a CT image and a voxelized sphere source of 20 mm-radius located inside the liver with a ^{99m}Tc activity of 150 MBq. Data were acquired within a primary energy window of 15% centered around the main photopeak of 140.5 keV and a lower scatter window of 15% centered around 120 keV — later used to correct scatter from acquired primary projections. Several sets of projections were generated, each consisting of 60 projections covering 360°, an acquisition time of 15 s per projection with 256 × 256 pixels of 2.39 mm spacing. The SPECT camera followed a circular orbit with a detector-to-center distance of 38 cm.

In this study, we considered a single rigid patient motion between two successive projections of the acquisition. The rigid patient motion was simulated by shifting simultaneously the attenuation and emission maps. One set of projections was simulated without motion and used as a reference. The performance of the motion detection and correction method was evaluated regarding:

1. Motion index: with a motion vector set to $(20,20,20)$ mm, all possible values of motion index (defined as the first frame index affected by motion), were evaluated.
2. Motion magnitude: with a motion index fixed at the middle of the acquisition, several motions were evaluated: 1, 3, 5, 10, 20 and 30 mm in all three axes.

2.3 eDCCs assessment

To replicate a clinical scenario with the CT image acquired only once before the SPECT acquisition, we used the attenuation map placed at the original position to compute eDCCs. We defined the convex K region covering the whole liver (created with auto segmentation of 3D Slicer on the CT image). To evaluate the consistency of the i-th and j-th SPECT projections p_μ with N detector lines in the axial direction, we employed the noise-aware metric [8, 12]

$$\mathrm{NE}_{p_\mu}(i,j) = \frac{\frac{1}{N}\sum_{l=1}^{N}|P(\theta_i,\sigma_{ij},z_l) - P(\theta_j,\sigma_{ji},z_l)|}{\sqrt{N}\sqrt{\mathrm{Var}(\overline{Pij}) + \mathrm{Var}(\overline{Pji})}} \tag{5}$$

with z_l the discretized z coordinate of the l-th line of the detector, the variance

$$\mathrm{Var}(\overline{P_{ij}}) = \frac{(\Delta s)^2}{N^2}\sum_{l=1}^{N}\sum_{k=1}^{M} C_l^2(\theta_i,s_k,z_l)p_\mu(\theta_i,s_k,z_l)e^{2\sigma_{ij}s_k} \tag{6}$$

Δs the pixel spacing and M the number of pixels per projection line.

According to findings in [8], rigid patient motion is the main contributor to projection inconsistency, i.e. high $\mathrm{NE}_{p_\mu}(i,j)$, whereas the physical effects have almost negligible (Poisson noise and collimator resolution) or moderate (scatter) impact on eDCCs.

To mitigate the effect of scatter on the motion estimation model, we applied scatter correction with the dual energy window (DEW) with a k factor of 1.1. The value of k was chosen to minimize the inconsistency in the reference motion-free acquisition. Then, a mask, defined as the forward projector of the K region, was applied to scatter-corrected frames after DEW to remove the remaining scattering from outside of the convex region.

2.4 Motion correction

If the patient's displacement is known, motion-free projections can be calculated by compensating for the patient's motion in the projection domain. When both the emission and attenuation maps are shifted by a vector in a transverse plane, the corresponding projections are shifted by a translation along the s-axis. Motion in an orthogonal direction, along the rotation axis z, can be directly interpreted as the same shift along the axial coordinate. Together, any 3D motion shift $\mathbf{a}$ can be corrected in the attenuated projection at a given detector angular position θ by a translation of the projection,

$$p_\mu^{\mathbf{a}}(\theta,s,z) = p_\mu(\theta, s+\mathbf{u}_\theta\cdot\mathbf{a}, z+\mathbf{e}_z\cdot\mathbf{a}). \tag{7}$$

2.5 Motion estimation

Let's define motion index m_0 as the first frame index affected by motion. m_0 divides the acquisition into no-motion projections $p_\mu(\theta_i,\cdot)$ for $i < m_0$ and motion-affected projections $p_\mu(\theta_j,\cdot)$ for $j \geq m_0$. Pairing projections in the second set with projections in the first set should result in non-zero eDCCs. In contrast, if these motion-affected projections $p_\mu(\theta_j,\cdot)$ are corrected by the true shift $\mathbf{a}_0$, the eDCCs should be closer to zero. To estimate m_0 and the shift $\mathbf{a_0}$, we therefore minimized the inconsistency between pairs of motion-corrected projections $p_\mu^{\mathbf{a}}$ of the two sets by solving the minimization problem

$$(\hat{m},\hat{\mathbf{a}}) = \underset{m\in\Omega_m,\,\mathbf{a}\in\mathbb{R}^3}{\operatorname{argmin}} F(m,\mathbf{a}) \tag{8}$$

with $\Omega_m = [2,L]$, L the number of projections within the acquisition, the cost function

$$F(m,\mathbf{a}) = \frac{1}{K}\sum_{i<m,j\geq m}\mathrm{NE}_{p_\mu^{\mathbf{a}}}(i,j) \tag{9}$$

and K the number of evaluated projection pairs (fulfilling $i < m \leq j$ and $|\theta_i - \theta_j| \neq 180°$).

The problem was solved by first calculating

$$\tilde{\mathbf{a}}_m = \underset{\mathbf{a}\in\mathbb{R}^3}{\operatorname{argmin}} F(m,\mathbf{a}) \tag{10}$$

for every $m \in \Omega_m$ with the Nelder-Mead downhill simplex algorithm [13] and then taking the value m that minimizes F, i.e., $\hat{\mathbf{a}} = \tilde{\mathbf{a}}_{\hat{m}}$ with

$$\hat{m} = \underset{m\in\Omega_m}{\operatorname{argmin}} F(m,\tilde{\mathbf{a}}_m). \tag{11}$$

2.6 Quantitative assessment of motion correction

The estimated motion shift was compared to the simulated value. For each projection set, the optimization was repeated 20 times with random initializations to estimate the robustness of the estimation.
The effect of motion correction on reconstructed SPECT images was visually assessed with a (20,20,20) mm shift occurring in the middle of the acquisition. The estimated motion was taken as the median of 20 random initializations. The motion-free projections, non-corrected projections and motion-corrected projections were reconstructed by the ordered subset expectation maximization (OSEM) implemented in RTK [14] using 5 iterations and 4 subsets with attenuation correction. The quality of reconstructed images was assessed via the activity recovery coefficient (ARC) in reference of the reconstructed SPECT images from motion-free projections

$$\mathrm{ARC}(\%) = \frac{A}{A_{\text{motion-free}}} \times 100\%. \tag{12}$$

The values A and $A_{\text{motion-free}}$ are the estimated activities in the source region obtained respectively from evaluated projections (non-corrected or motion-corrected projections) and from motion-free projections taken as reference.

3 Results

The ability to detect a $(20,20,20)$ mm translation appearing at different motion indices of the acquisition is shown in Fig. 1. Plot A indicates the values of the cost function after optimization for every position $m \in [2,60]$, i.e., $F(m, \tilde{\mathbf{a}}_m)$, while B shows the difference between the estimated $\hat{m}$ and the true motion index m_0 for all possible $m_0 \in \Omega_m$ with two selected examples of motion magnitude. For a 20 mm motion per axis (blue curve in Fig. 1B), the motion index was adequately estimated. For 3D motions below 5 mm per axis, for instance the black curve in Fig. 1B, $\hat{m} - m_0$ was not zero, i.e., the estimation of the motion index was incorrect for several values of m_0.

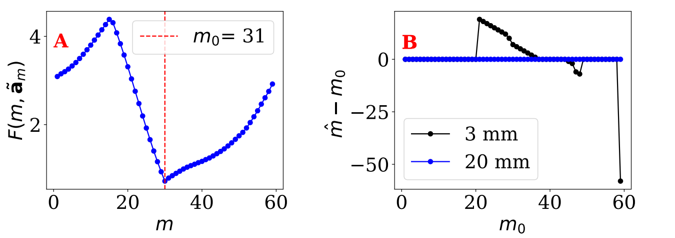

Figure 1: A. Illustration of motion detection with sliding value $m \in [2,60]$ for (20,20,20) mm displacement in the middle of acquisition; B. Performance of motion detection for different motion indices m_0 with respectively (20,20,20) mm shift (blue) and (3,3,3) mm (black).

Fig. 2 illustrates the estimation of (20,20,20) mm translation occurring at different motion index m_0 along the acquisition. The proposed method returned promising accuracy where the absolute differences were close to or below the pixel size of 2.39 mm for each direction. There was also a significant precision at the sub-millimeter level across different repetitions of the optimizer, with only a minor number of outliers.

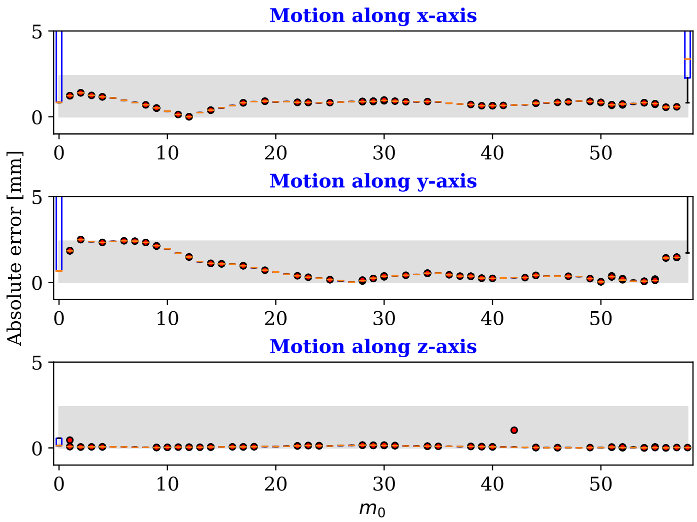

Figure 2: Box and whisker plot (blue) for absolute error of motion estimation at different motion indices m_0 for $\mathbf{a}_0 = (20,20,20)$ mm. Horizontal red lines inside the box represent the median value and circular red dots are outliers with high bias, i.e. values greater than 1.5 inter-quartile range.

In general, motion assessment along z was highly accurate with an error below 1 mm. The mean deviation for all values of motion index m_0 was around 0.05 mm in this axis compared to respectively 1.4 and 2.2 mm in x and y. Also, misestimation in x and y were generally synchronous.
For smaller shifts below 5 mm, the absolute relative errors were larger (data not shown), e.g., up to 10 to 50 % compared to the true values for mid-acquisition motion. When the shift is above 5 mm per axis, these errors are below 10% for all three components. These findings are consistent with the results above.
The ARC before and after motion correction is shown side-by-side in Fig. 3. Without correction, the values of ARC spread in a wide range from 15% to nearly 100%. In contrast, motion correction brought a comparable ARC to motion-free images, i.e. less than a 5% drop for motion occurring early in the acquisition and below 1% for motion occurring after one-third of the acquisition.
The improvement in the reconstructed image is illustrated in Fig. 4. Motion correction greatly mitigated the artifacts, namely blurring and distortion of the sphere.

4 Discussion

In this study, eDCCs were exploited to detect and correct for rigid patient motion in SPECT projections simulated with Monte Carlo simulations using a realistic SPECT scanner model.

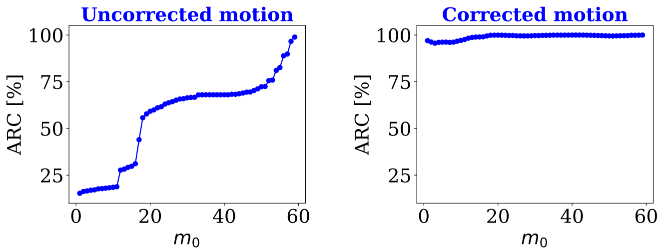

Figure 3: Activity recovery coefficient (ARC) as a function of motion index m_0 for $\mathbf{a}_0 = (20, 20, 20)$ mm.

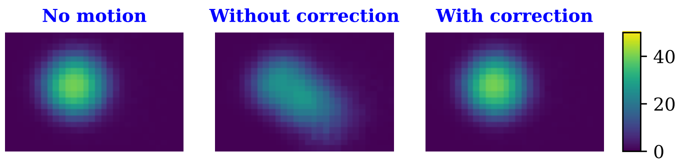

Figure 4: Visualization of reconstruction with motion-free, non-corrected, and motion-corrected projections for $m_0 = 31$ and $\mathbf{a}_0 = (20, 20, 20)$ mm.

The current two-step procedure first showed the reliability of detecting sudden inter-frame translation of (20,20,20) mm happening between any two successive frames of the acquisition, i.e. different possibilities of m_0. For the sliding value of $m \in [2, 60]$, frames after m were corrected simultaneously with the same shift to optimize projection consistency. If $m \neq m_0$, some motion-free ($p(\theta_i, \cdot)$ for $i < m_0$) or non-corrected ($p(\theta_j, \cdot)$ for $j \geq m_0$) projections are wrongly motion-corrected or non-corrected, respectively, and both raised the inconsistency in the cost function (Fig. 1A).
For a known motion index m_0, the motion correction performed on projections from Monte Carlo simulation already achieved quite good agreement with true values. In general, estimation on the z-component, which was independent of motion index m_0, surpassed those in the other two directions in terms of accuracy. Indeed, translation in z is more sensitive to eDCCs than in the other two directions since it directly correlates to the same translation for all angular positions of the detector θ_m.
In good agreement with the findings from Robert *et al.* [8], we observed that the collimator resolution and Poisson noise had a minor impact on the correction of motion with eDCCs using scatter-free simulations obtained by RTK ray tracing modeling these two effects [14] (data not shown). On the contrary, the presence of scatter in the Monte Carlo simulation noticeably degraded the accuracy of our proposed correction method when no scatter correction was performed (data not shown).

5 Conclusions

Rigid patient motion in SPECT has been detected and corrected with an algorithm exploiting exponential data consistency conditions. A two-step process was shown to be practical for SPECT measurements simulating all physical effects which is promising for future application to real scanner data.

References

[1] T. Wheldon and J. O'Donoghue. "The Radiobiology of Targeted Radiotherapy". *International Journal of Radiation Biology* 58.1 (1990). PMID: 1973428, pp. 1–21. DOI: 10.1080/09553009014551401.

[2] A. K. Buck, S. Nekolla, S. Ziegler, et al. "SPECT/CT". *Journal of Nuclear Medicine* 49.8 (2008), pp. 1305–1319. DOI: 10.2967/jnumed.107.050195.

[3] J. Imbrescia, G. Volpi, S. Lucchini, et al. "A Brief Report on the Role of SPECT/TC in the Optimization of Radiotherapy Treatment with Radical Intent for Unresectable Stage III NSCLC". *Applied Sciences* 12.18 (2022). DOI: 10.3390/app12189351.

[4] J. A. Christian, M. Partridge, E. Nioutsikou, et al. "The incorporation of SPECT functional lung imaging into inverse radiotherapy planning for non-small cell lung cancer". *Radiotherapy and Oncology* 77.3 (2005), pp. 271–277. DOI: https://doi.org/10.1016/j.radonc.2005.08.008.

[5] J. Wheat and G. Currie. "Incidence and characterization of patient motion in myocardial perfusion SPECT: part 1". English. *Journal of Nuclear Medicine Technology* 32.2 (2004), pp. 60–65.

[6] A. Z. Kyme and R. R. Fulton. "Motion estimation and correction in SPECT, PET and CT". *Physics in Medicine & Biology* 66.18 (Sept. 2021), 18TR02. DOI: 10.1088/1361-6560/ac093b.

[7] R. G. Wells and R. Clackdoyle. "Feasibility of attenuation map alignment in pinhole cardiac SPECT using exponential data consistency conditions". *Medical Physics* 48.9 (2021), pp. 4955–4965. DOI: https://doi.org/10.1002/mp.15058.

[8] A. Robert, D. Sarrut, A. Etxebeste, et al. "Ability of exponential data consistency conditions to detect motion in SPECT despite other physical effects". *17th International Meeting on Fully 3D Image Reconstruction in Radiology and Nuclear Medicine, Stony Brook, NY, USA* (2023).

[9] F. Natterer. *The Mathematics of Computerized Tomography*. NY: John Wiley & Sons, 1986.

[10] D. Sarrut et al. "Advanced Monte Carlo simulations of emission tomography imaging systems with GATE". *Phys Med Biol* 66.10 (May 2021), 10TR03. DOI: 10.1088/1361-6560/abf276.

[11] M. Bui, A. Robert, J. Badel, et al. "Validation of a model of the Symbia Intevo Bold SPECT scanner for Monte Carlo simulations". *2023 IEEE Nuclear Science Symposium, Medical Imaging Conference and International Symposium on Room-Temperature Semiconductor Detectors (NSS MIC RTSD)*. 2023, pp. 1–1. DOI: 10.1109/NSSMICRTSD49126.2023.10338340.

[12] M. Mouchet, J. M. Létang, J. Lesaint, et al. "Cone-beam pair-wise data consistency conditions in helical CT". *IEEE Transactions on Medical Imaging* (2023), pp. 1–1. DOI: 10.1109/TMI.2023.3265812.

[13] J. A. Nelder and R. Mead. "A Simplex Method for Function Minimization". *The Computer Journal* 7.4 (Jan. 1965), pp. 308–313. DOI: 10.1093/comjnl/7.4.308.

[14] S. Rit, M. Vila Oliva, S. Brousmiche, et al. "The Reconstruction Toolkit (RTK), an open-source cone-beam CT reconstruction toolkit based on the Insight Toolkit (ITK)". *Journal of Physics: Conference Series* 489 (Feb. 2014). DOI: 10.1088/1742-6596/489/1/012079.